


Free fall of homogeneous and heterogeneous conesJin-Tae Kim,¹ Yaqing Jin,² Shikun Shen,¹ Ankan Dash,¹ and Leonardo P. Chamorro ^{1,3,4,*}¹*Mechanical Science and Engineering Department, University of Illinois, Urbana, Illinois 61801, USA*²*Mechanical Engineering Department, The University of Texas at Dallas, Richardson, Texas 75080, USA*³*Civil and Environmental Engineering Department, University of Illinois, Urbana, Illinois 61801, USA*⁴*Aerospace Engineering Department, University of Illinois, Urbana, Illinois 61801, USA*

(Received 7 April 2020; accepted 2 September 2020; published 24 September 2020)

The late stage of the free fall of homogeneous and heterogeneous cones in a quiescent water medium and the induced flow are experimentally inspected using three-dimensional particle tracking velocimetry and volumetric particle image velocimetry. The structures shared the same geometry but had different combined specific gravity $SG \in [1.2, 8]$. Results showed four distinct free-fall patterns, which were modulated by the degree of heterogeneity and SG . They included (i) straight fall, (ii) regular sinusoidal-like trajectories with a maximum angle of oscillation with respect to the vertical, $\theta_{\max} < \pi/2$, (iii) motions characterized by inclined translations and large rotations with $\theta_{\max} > \pi/2$, and (iv) tumbling followed by an irregular motion. The straight fall occurred in cones with $SG \gtrsim 6$ regardless of the mass distribution. The sinusoidal motions arose in the homogeneous cones with $SG < 3$. The large rotations occurred with heterogeneous cones of $SG < 3$, whereas the tumbling with irregular motions occurred in the heterogeneous cone with the highest ratio between the center of mass and geometrical centroid. Inspection of the linear and angular components of the velocities and accelerations reveal the distinct patterns and the linkage with the surrounding flow.

DOI: [10.1103/PhysRevFluids.5.093801](https://doi.org/10.1103/PhysRevFluids.5.093801)**I. INTRODUCTION**

Body free fall is an overwhelmingly common phenomenon, which has been investigated over a long time due to the implications and applications in nature and engineering, e.g., parachute landing [1], settling of volcanic ashes [2], and seed spreading [3]. The Lagrangian features of a gravity-driven falling object depend on multiple parameters, including the geometry, stiffness, and heterogeneity of the structure as well as the medium and relative flow (flow with respect to the body), among others.

The interaction between flow and falling objects may be extremely complicated; many distinct patterns may arise with relatively minor changes in the structure or surrounding flow. Substantial efforts have been made in describing the shed vortices and the mechanisms modulating the fluid-body interaction to gain insight into the trajectory patterns, drag, and control strategies, among other phenomena. Over a century ago, Maxwell [4] discussed the falling of flexible plates. Early experimental studies using dye visualization focused on the wake of falling bodies, including liquid droplets [5], spheres [6], cylinders [7], and circular disks [8]. They noted the formation of distinct vortex rings under sufficiently large Reynolds numbers, and the possibility of oscillatory motions.

*Corresponding author: lpchamo@illinois.edu

During the last decades, several studies have explored the falling of axisymmetric objects; geometry simplicity facilitates the theoretical treatment and serves to increase understanding of complex geometries. Numerical and experimental efforts [9–11] have shown the influence of the mass ratio and Re on the dynamics of free-falling spheres and the shed vortical structures, where multiple vortex rings may be induced within a cycle of zigzag oscillation when it occurs. Circular thin disks present complex flow dynamics due to the distinct effects of the angular movements. Field *et al.* [12] performed experimental observations of disks falling in water and glycerol mixtures and reported four different types of disk dynamics, namely, steady falling, periodic-oscillating, chaotic, and tumbling motions. Zhong *et al.* [13] systematically investigated the wake-structure coupling of disk zigzag motions; they reported that the transition from planar zigzag to nonplanar spiral movements occurs when the vortex structure changes from hairpin to a pair of counter-rotating helicoidal shape vortices. A following work by Zhong *et al.* [14] showed that a dipole vortex substantially different from the classical Kármán type might be created at sufficiently high Re . Kanso *et al.* [15] investigated coins falling in water and identified four types of trajectories governed by the moment of inertia and Reynolds number. Vincent *et al.* [16] explored the motion of thin disks with a central hole and noted that the dynamics of disks may transit from tumbling to chaotic and finally fluttering motions with the size increase of the central hole. Recently, Lam *et al.* [17] studied passive motions of falling discs under density-stratified media; they noted that the density stratification significantly decreased the vertical descent speed, fluttering amplitude, and body inclination.

Comparatively, fewer studies have focused on falling cones. Early experimental work by Calvert [19] explored the wake, turbulence-induced characteristics, and pressure distribution on cones with various apex angles; he found similar wakes and suggested that the Strouhal number may characterize the wake fluctuations. Yaginuma and Ito [20] explored multiple free-falling cones with an apex angle of 60° at Re within 90 to 8×10^3 and noted ring-shaped hairpin vortices within $100 < Re < 400$ via dye visualizations. Hamed *et al.* [21] studied the transient dynamics of free-falling cones for various apex angles; they found a critical Re leading to rapid growth in the cone nutation and deviation from the vertical axis. Results highlighted the presence of symmetric three-dimensional (3D) vortex rollup in the early stage of the fall. Recently, Amin *et al.* [22] investigated the free falling of cones with various apex angles and reported that dynamics of homogeneous cones may exhibit inversion, tumbling, gliding, oriented flight, rocking, and fluttering with the increase of the apex angle. Other studies have inspected the free fall in complex fluids. For instance, Sharma and Chhabra [23] showed that the wall effect and drag coefficient of free-falling cones may present significant differences under Newtonian or non-Newtonian fluids. Recently a numerical work by Mishra *et al.* [24] pointed out the positive dependence between the drag coefficient and the Bingham number for a cone settling in a Bingham plastic fluid.

The complex fluid-structure coupling (FSC) of free-falling structures is not well understood. The study of bodies of reduced complexity is instrumental in understanding the FSC phenomenon in generalized scenarios; cones are one of such geometries. So far, most of the efforts have focused on bodies with homogeneous densities where the gravity and geometric centers coincide. Nonhomogeneous structures sharing the geometry may undergo distinct dynamics; there, the relative position of the center of gravity and center of mass may play a dominant role in the fall, oscillations, and wake dynamics. Understanding the free falling of heterogeneous objects is also instrumental for the design of autonomous underwater vehicles (AUV) [25,26] and parachute systems [1,27], among others. Here, we experimentally explore the fluid-structure coupling of free-falling cones sharing the same geometry but different density ratios and centers of gravity. 3D particle tracking velocimetry (PTV) and high-speed 3D particle image velocimetry (PIV) are used to uncover the coupling between cone motions and induced flow characteristics. The study also provides insight into the parameters determining the dominant dynamics, which is needed for a comprehensive assessment of the phenomenon.

The study is organized as follows: the experimental setup is described in Sec. II, the results and analysis are discussed in Sec. III, and the conclusions are summarized in Sec. IV.

II. EXPERIMENTAL SETUP

The late stage of the free fall of three homogeneous and six heterogeneous cones sharing the same dimensions was characterized in a quiescent medium. Before the onset of motions, the cones were submerged about three diameters below the free surface of a cubic, clear-acrylic tank of 1200 mm height and 300 mm \times 300 mm cross section. The cones had a height of $h = 10$ mm and a diameter of $d = 20$ mm, implying an apex angle of $\alpha = 90^\circ$. The structures were made with the combination of two materials, resulting in relative densities or specific gravities ranging from $SG = \rho/\rho_w = 1.2$ to 8, where ρ and ρ_w are the average densities of the cones and water. The homogeneous cones were made of acrylic ($\rho_1 = 1.2 \text{ g cm}^{-3}$), aluminum ($\rho_2 = 2.7 \text{ g cm}^{-3}$), and stainless steel ($\rho_3 = 8.0 \text{ g cm}^{-3}$). Three heterogeneous cones were made with combinations of acrylic and stainless steel, and the other three heterogeneous cones included combinations of acrylic and aluminum. In these structures, the lightest material was located at the top, near the apex portion, as illustrated in Fig. 1(a). We note that a more extensive set of cases would have helped to determine and characterize more precisely each distinct dynamics. However, the selected scenarios show the possible patterns experienced by the cone falling.

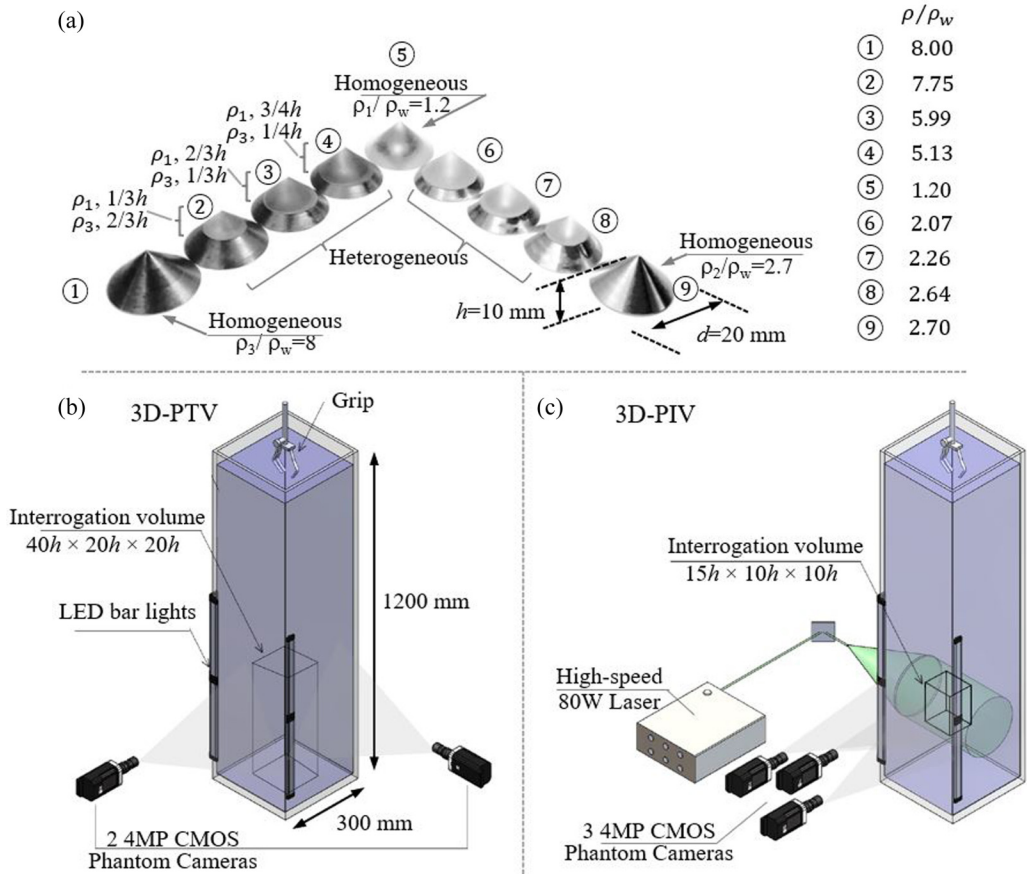


FIG. 1. (a) Characteristics of the nine cones; ①, ⑤, and ⑨ indicate the homogeneous structures. (b) Schematic of the experimental setup for the tracking of the cones using 3D particle tracking velocimetry (3D-PTV). (c) setup for the characterization of the induced 3D flow field via 3D particle image velocimetry (3D-PIV).

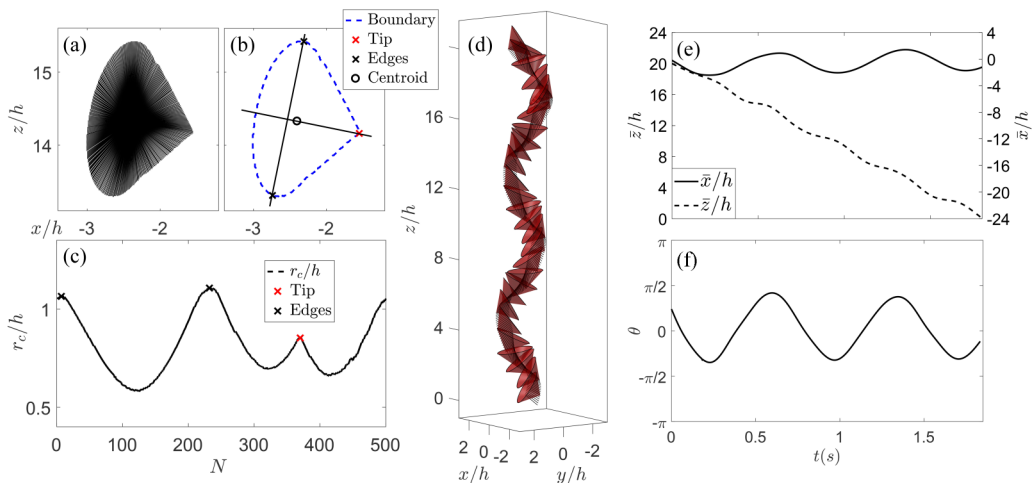


FIG. 2. Illustration of the 3D posture reconstruction. (a) Boundary recognition, (b) detection of tip and edges based on the boundary and centroid (black circle), and (c) distances between the centroid and the boundary, r_c ; global and local peaks indicate the edges (black cross) and tip (red cross). (d) Sequence of a falling cone 5, (e) evolution of the horizontal (\bar{x}) and vertical \bar{z} locations of the cone centroid, and (f) inclination angle from the vertical.

The cones are labeled with numbers 1 to 9 for easier reference in later discussion; details of the geometry of these structures are given in Fig. 1(a). Basic schematics of the experimental setup that includes the 3D-PTV and 3D-PIV are shown in Figs. 1(b) and 1(c). The tank was filled with an 1150 mm column of clear distilled water. Before releasing each cone from a three-hand arm, the setup was kept undisturbed for at least twenty minutes to minimize the induced flow perturbations. Each experiment was repeated five times to ensure the proper functionality of the dropping mechanism and minimize the likelihood of any unwanted changes in the initial condition. Details of the tracking of the cones and characterization of the induced flow are given as follows.

A. Body kinematics via 3D-PTV

Two synchronized CMOS 4-megapixel cameras were mounted perpendicularly to track the motion of the cones within an interrogation volume spanning 400 mm in the vertical and 200 mm in each horizontal coordinate. The interrogation volume was located at the center of the tank, near the bottom; it was sufficient to cover at least three cycles of the observed cone oscillations. It is worth noting that the cones were allowed to travel over $70h$ before reaching the interrogation volume to remove initial transient effects. The cones were coated with a very thin layer of white spray paint to improve the tracking. Six LED light bars were mounted at two corners of the tank to illuminate the interrogation volume; this removed the cone shadows in the two camera views. The perpendicular image pairs were captured at a sampling frequency of 300 Hz, which was sufficient to describe the motion of the cones.

The 3D position and orientation of the falling cones at a given instant were inferred from the principal axis connecting the cone tip and geometrical centroid of the structure and processed as follows. After preprocessing image sequences, such as removal of the background noise, the projection of the cone center and orientation to each camera plane were measured and tracked by tracing the boundaries of the cones [Fig. 2(a)]. To obtain the principal axis, it is essential to locate the cone tip and the location of the two edges, i.e., the farthest points from the axis. The distance between the geometrical centroid and each boundary point, r_c , was computed and used to identify instantaneous locations of edges and tip; there, two points from the maximum and one point

from the local maximum gave two edge points and the tip point [Fig. 2(c)]. The orientation of the principal axis and the projected length of the distance between the tip and centroid with respect to the two perpendicular camera view planes allowed for calculating the 3D orientation of the principal axis. The kinematics of a falling cone can then be reconstructed with the instantaneous angle and location of the 3D principal axis. The 3D principal axes during the fall were tracked using the nearest method and linked by performing a three-frame gap closing for reconstructing a complete trajectory throughout the measurement sequence. Temporal derivatives of the cones' trajectories and angles were evaluated and filtered using fourth-order B-splines [28].

An example of the structure tracking capturing the principal axis and oscillation of cone 5 is illustrated in Fig. 2(d) with superimposed snapshots. Temporal evolution of the displacement of the cone centroid in the horizontal \bar{x} and vertical \bar{z} directions as well as the inclination angle are shown in Figs. 2(e) and 2(f). More details of image detection and tracking method can be found in Kim *et al.* [29–31].

B. Induced flow via 3D-PIV

Complementary measurements with three-dimensional particle image velocimetry from TSI were performed to characterize the induced flow and dominant vortical motions that modulated the distinct movements of the cones. The system consisted of three 2560×1600 pixel CMOS Phantom Miro 340 cameras with 12 GB onboard memory and a high-speed 50 mJ dual cavity YLF laser from Terra. The cameras focused on an interrogation volume of 150 mm height and $100 \text{ mm} \times 100 \text{ mm}$ cross section, which was located near the bottom of the tank and seeded with silver-coated glass spheres of $55 \mu\text{m}$ diameter and 1.05 specific gravity. The selected investigation volume covered at least 1.5 cycles of the cone oscillations. The 3D image sets were interrogated using a recursive cross-correlation method via the Insight 4G software from TSI.

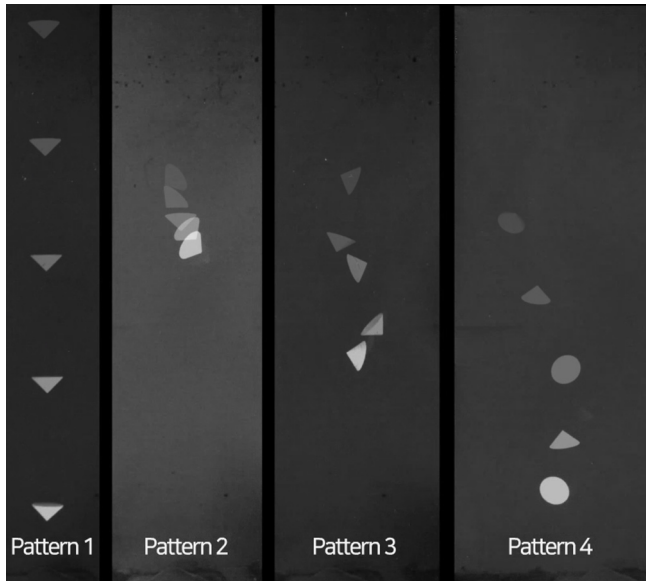


FIG. 3. Distinct patterns exhibited by the cones. Pattern 1: straight fall; Pattern 2: regular sinusoidal-like trajectories with a maximum angle of oscillation $\theta_{\max} < \pi/2$; Pattern 3: with large rotations $\theta_{\max} > \pi/2$ with inclined translations; and Pattern 4: tumbling followed by irregular trajectory. Superimposed images every $\Delta t = 0.1$ s. See Supplemental Material at [18] for visualization of the motions.

III. RESULTS

The free fall of the cones past the initial transient behavior exhibited four distinct patterns modulated by the degree of heterogeneity and the bulk specific gravity; see superimposed raw images every $\Delta t = 0.1$ s in Fig. 3.

A straight fall characterized one of the patterns (Fig. 3, Pattern 1), which occurred in cones with high specific gravity of $\rho/\rho_w \gtrsim 6$ regardless of the mass distribution (cones 1, 2, and 3; see Fig. 1). There, the cones did not experience acceleration and angular motion. Regular sinusoidal-like trajectories with body oscillations with angle of rotation $\theta_{\max} < \pi/2$ described another distinct pattern (Fig. 3, Pattern 2). These cases occurred in the homogeneous cones with a density of $\rho/\rho_w < 3$ (cones 5 and 9). The third pattern was characterized by inclined translation and large rotations with $\theta_{\max} > \pi/2$ (Fig. 3, Pattern 3); it occurred with heterogeneous cones of $\rho/\rho_w < 3$ (cones 6, 7, and 8). The fourth pattern exhibited tumbling followed by irregular motions (Fig. 3, Pattern 4); it occurred with the cone that has the largest distance between the center of mass and tip $h_c/h = 0.85$ (cone 4). See also the Supplemental Material at [18], which illustrates the four distinct motion patterns.

Cones 1, 2, and 3 ($\rho/\rho_w = 8.00, 7.75,$ and 5.99) experienced nearly straight trajectories, with negligible inclinations and oscillations [see Fig. 1(a)]. The basic features of the fall are illustrated in Fig. 4(a). There, the vertical displacement increased linearly with time. This trend also indicates a fall with a terminal velocity, u_s , which is shown normalized by that of cone 1 ($\rho/\rho_w = 8$), $U = 0.783$ m s⁻¹ in the inset. The Reynolds numbers for those straight fall cases were $\text{Re} = 1.65 \times 10^4$, 1.57×10^4 and 1.38×10^4 . The straight trajectory induced a flow [Fig. 4(b)] that facilitated the development of vortex rings as shown in Fig. 4(c), which are illustrated with isocontours of Q criterion ($Q = 0.02$ and -0.04 s⁻¹). This quantity is defined as the local balance between shear strain rate $\|S\|$ and vorticity magnitude $\|\Omega\|$: $Q = \frac{1}{2}\|\Omega\|^2 - \|S\|^2$. Vortical structures were induced by the relatively strong shear layer developed between the induced flow in the wake and the negligible motions outside the wake. Hamed *et al.* [21] showed that these structures are induced from Kelvin-Helmholtz-like instability. Lack of symmetry due to, e.g., minor inclinations of the

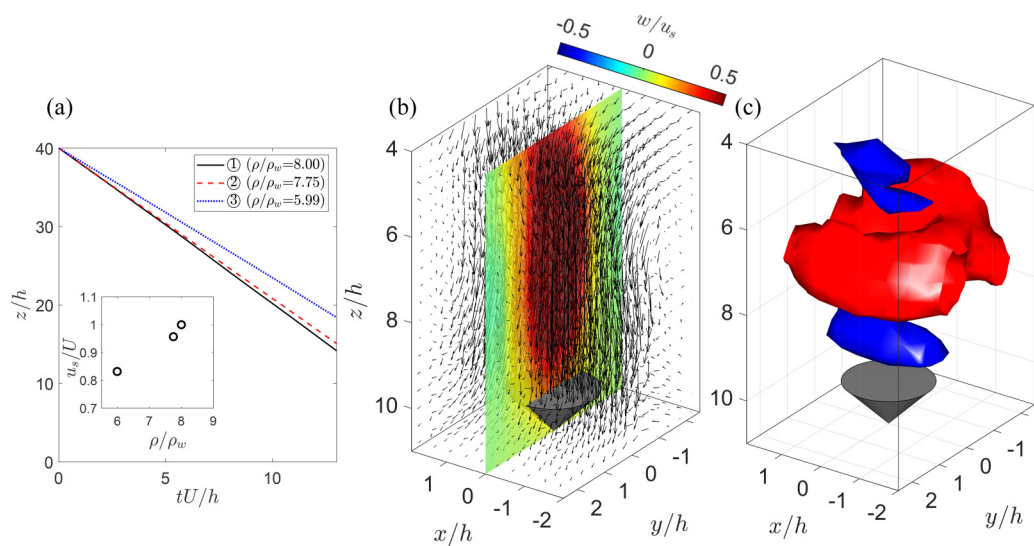


FIG. 4. (a) Stable free fall for $\rho/\rho_w \geq 6$ cones; the inset shows terminal velocity u_s , normalized by the terminal velocity of $\rho/\rho_w \geq 8$, U . (b) 3D flow field of a stable fall; w is the vertical component of the flow velocity. (c) Q criterion; red and blue isosurfaces denote shed structures (with $Q = 0.02$ s⁻¹ and $Q = -0.04$ s⁻¹).

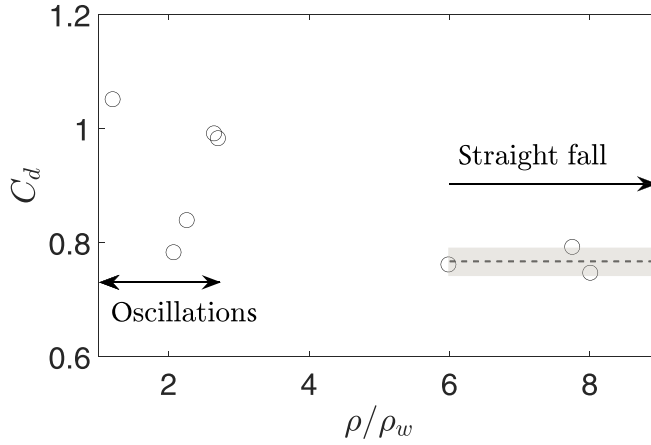


FIG. 5. Drag coefficient C_d of the cones with straight fall as a function of ρ/ρ_w . Also included is the bulk estimation over one cycle for those cases with periodic oscillations.

cone and Reynolds number may induce the vortex breakdown, which imposes asymmetrical forces on the structure that may lead to unsteady trajectories.

The straight fall with terminal velocity allows estimating the drag coefficient, C_d , by accounting the balance between drag, gravity, and buoyancy forces. Taking the base area as a reference, C_d is

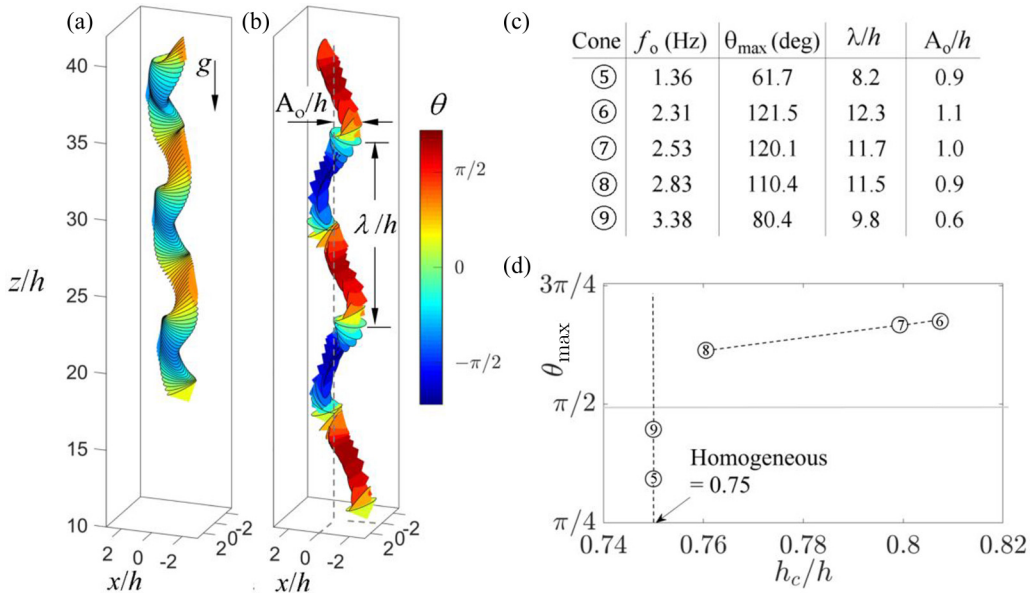


FIG. 6. 3D trajectories of the (a) homogeneous cone 5 and (b) heterogeneous cone 6. (c) Summary table including frequency of oscillations f_o , maximum inclination angle θ_{\max} , wavelength λ , and amplitude A_o of the trajectories. (d) Basic relation between θ_{\max} and degree of heterogeneity h_c/h . h_c is the center of mass, the distance from the apex along the cone axis; note that the geometric center and center of mass coincide when $h_c/h = 0.75$ (homogeneous cones).

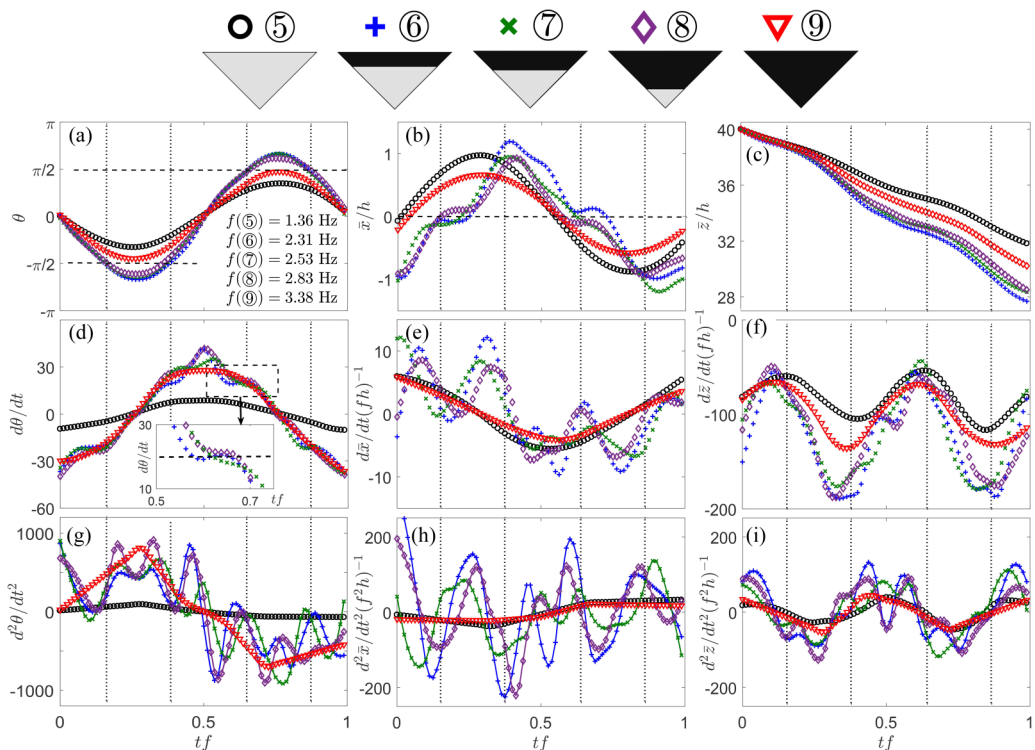


FIG. 7. Kinematics of the cones that exhibited regular oscillations, and large rotations with inclined translations. Temporal evolution of the (a) angle θ with respect to the vertical, (b) lateral displacement \bar{x} , (c) vertical displacement \bar{z} . (d)–(f) Corresponding velocities and (g)–(i) corresponding accelerations.

given by

$$C_d = \frac{2h(\rho/\rho_w - 1)g}{3u_s^2}, \quad (1)$$

i.e., $C_d \approx 0.77$ for the cones under straight fall (Fig. 5), which approximately matches known values for 90° -apex-angle cones [32,33].

A reduction of the density to $\rho/\rho_w < 3$ significantly altered the dynamics of the cones and wake characteristics; there, distinct oscillations dominated the motions of the fall. Following Eq. (1), Fig. 5 shows the bulk drag coefficient of all cones as a function of ρ/ρ_w in a representative cycle. The cone oscillations led to higher C_d compared to the straight fall. As discussed next, the projected area of oscillating cones in the motion plane varies continuously, and the cones may exhibit lateral movements. This led to significant periodic changes in the forces acting on the cones.

The trajectory patterns characterized by regular oscillations ($\theta_{\max} < \pi/2$) and large oscillations ($\theta_{\max} > \pi/2$) with short inclined translations were significantly affected by the specific gravity and the degree of heterogeneity (see Fig. 3, Pattern 3, and Supplemental Material at [18] for details). Figures 6(a) and 6(b) illustrate superimposed snapshots for one of each of these cases, namely, the lightest homogeneous case (cone 5) and a heterogeneous case (cone 6). For completeness, a summary of the frequency of the oscillations, f_o , maximum θ , wavelength of the trajectory oscillations, λ , and the amplitude of motions, A_o , are shown in Fig. 6(c) for the cones 5 to 9, which underwent these two oscillatory patterns. Figure 6(d) provides a basic assessment of the impact of mass distribution, h_c/h , on the maximum oscillation angle; there, note that $h_c/h = 0.75$ in the homogeneous cones.

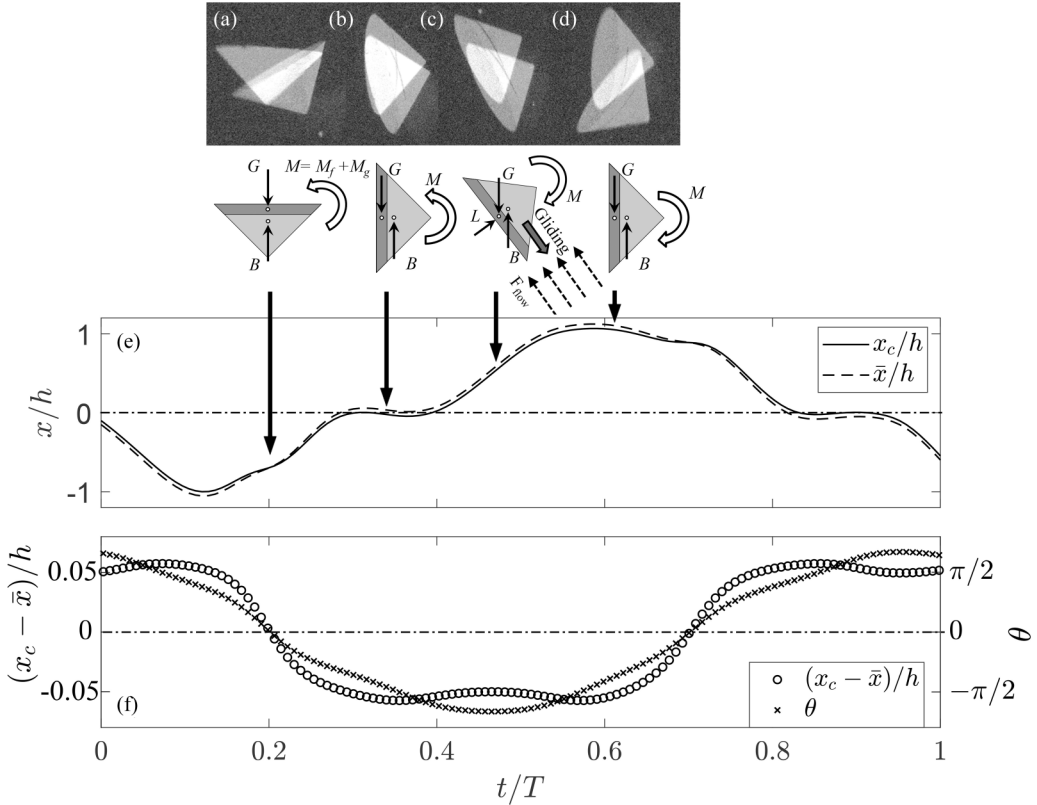


FIG. 8. Superimposed pair of raw images of the heterogeneous cone 6 at various fall instants: (a) no inclination, (b) large rotation, (c) inclined translation (gliding), and (d) backward rotation; G , B , M_f , M_g , M , and L denote the gravity force acting on the center of mass, buoyancy force acting on the centroid, base torque, additional torque (misalignment between G and B), total torque, and lift. (e) Location of the centroid, \bar{x} , and center of mass, x_c with respect to the mean fall axis. (f) Difference between \bar{x} and x_c and oscillation angle. θ .

The distinct periodic oscillations of these motions (cones 5 to 9) modulated temporal changes of θ and linear and angular velocities and accelerations, resulting in complex dynamics within a representative cycle. To facilitate a comparison of these quantities, Fig. 7 shows the various cases normalized within one oscillation period. Despite the significant density difference in the homogeneous cones 5 and 9, their dynamic patterns are qualitatively similar, i.e., both angular and linear motions presented a sinusoidal-like motion dominated by a single frequency. It is worth pointing out that the maximum vertical acceleration occurred approximately at the same instant when $|\theta|$ reached the maximum [Figs. 7(a) and 7(i)]. Results indicate that high inclination angle reduced the projected area in the vertical direction and, therefore, produced reduced instantaneous drag. The heterogeneous cones experienced much more complex dynamics, where secondary oscillations are distinctive in both angular and linear motions. Indeed, within the large rotations [$|\theta| > \pi/2$ in Fig. 7(a)], the base of the cone necessarily faced a relative flow (discussed next), where the form drag increased. This is reflected in Fig. 7(i) with a fast increase of d^2z/dt^2 .

Due to its frequent occurrence in nature and implication in engineering, it is worth additional inspection of the underlying process experienced by the cones under significant rotation and inclined translation, shown in Fig. 8 for cone 6. The symmetry break of vortex shedding is expected to produce unbalance on the pressure acting on the base of the cone, and a differential change in the

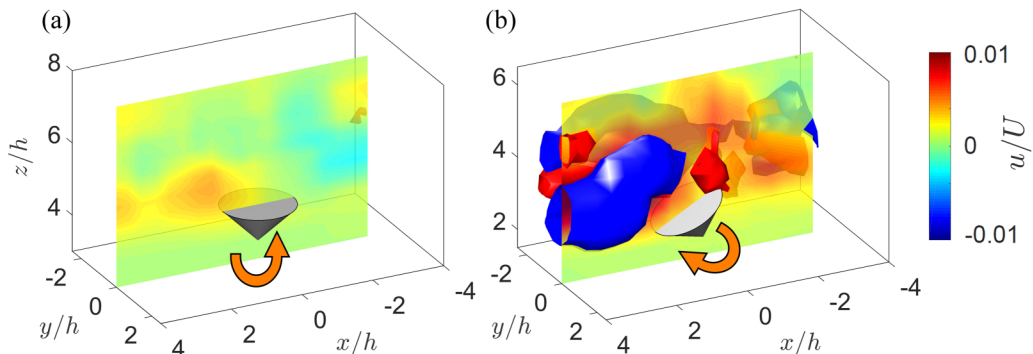


FIG. 9. Horizontal velocity induced by the homogeneous cone 5 with superimposed velocity vectors at (a) no and (b) maximum inclinations. Isocontours of the Q criterion ($= 0.01$, and -0.04 s^{-1}) are included for reference.

symmetry of the torque (M_f) at the base of the structure; it eventually triggered the cone oscillation [Fig. 8(a)]. Flow features around the cone shown in Fig. 9 are discussed later. See also Hamed *et al.* [21] for complementary insight on the flow around the base of the structure. Cone inclination led to $|\bar{x} - x_c| > 0$, i.e., the center of buoyancy (\bar{x}) and center of mass x_c were not aligned vertically. Due to the opposite direction of gravity and buoyancy, additional torque (M_g) is produced in the same direction of M_f . The combined torque $M_f + M_g$ promoted further oscillation and inclination angle with eventually $\theta > \pi/2$ for specific mass distributions [Fig. 8(b)]. Under sufficiently high rotation, the base of the cone faced a relative flow due to cone motion. This resulted in a net lift, which contributed to the cone gliding and associated deviation from the vertical falling axis [Fig. 8(c)]. It led to a comparatively fast increase of x_c/h [see Fig. 8(e)]. Under high inclination and gliding motion, the lateral side of the cone was impinged by the relative flow. Due to the larger lateral area closer to the cone base, the base torque acted in the opposite direction of θ . This prevented the increase of θ ; then, the cone returned to the initial stage, which was followed by a new oscillation cycle. In cone 4, a comparatively large M_g was generated due to the large difference between the center of mass and geometrical centroid ($h_c/h = 0.85$). This resulted in turnovers and irregular tumbling motions.

The flow induced by the heterogeneous cones experiencing oscillations with or without gliding is undoubtedly complex. We show representative instants of two cases with regular ($\theta_{\max} < \pi/2$, cone 5) and large ($\theta_{\max} > \pi/2$, cone 6) oscillations in Figs. 9 and 10; they illustrate the particular coupling between the cones and flow. The heterogeneous light cone 6 induced stronger wake than the case of homogeneous light cone 5 due to the higher terminal velocity, u_s . At a negligible inclination angle, the induced horizontal velocity component for both cases [cone 5, Fig. 9(a), and cone 6, Fig. 10(c)], pushed the cone to rotate in the counterclockwise direction. It is worth noting that the case with large oscillation (cone 6) induced faster relative flow, which was promoted by the gliding. Indeed, during the gliding stage, the cone induced a flow along the gliding direction near the base [Fig. 10(a), III] and flow against the gliding course over the base [Fig. 10(a), II]. These flow structures are developed until the onset of backward rotation [Fig. 10(b)], where the structure III, which moved towards the apex, induced additional torque and contributed to the change in the rotation direction. This is in addition to the relative fluid force in front of the cone's falling course [I in Fig. 10(b)], as discussed in the previous section. Also interesting is the detached structure II [Fig. 10(b)]; it is a flow relatively opposite to the direction of the cone. This phenomenon may promote mixing due to a combination of large oscillation amplitude and large wake structure that propagates out of the gliding direction. Around the maximum rotation over $\pi/2$,

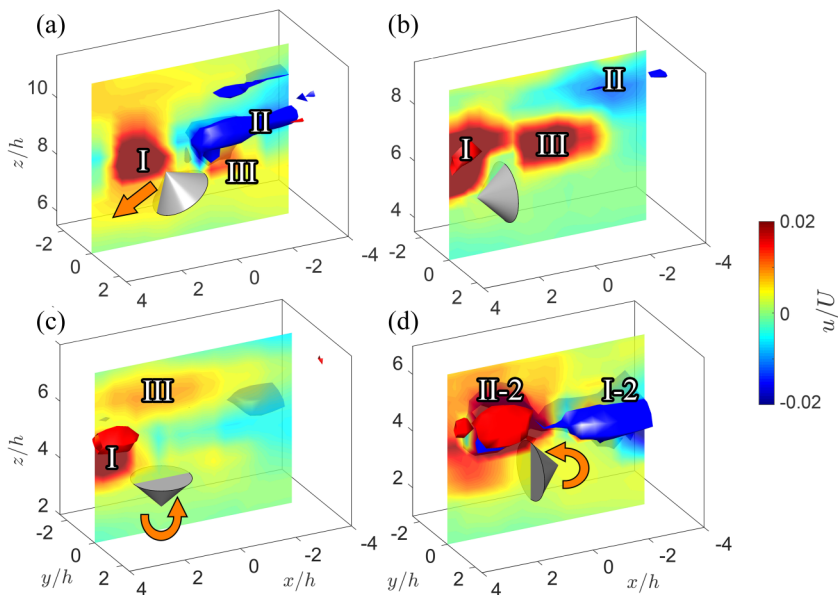


FIG. 10. 3D flow fields of a heterogeneous light cone (case 6) at (a) gliding, (b) rerolling, (c) 0° inclination angle, and (d) over-rolling with in-plane contours indicating horizontal velocity. Isocontours of the Q criterion ($= 0.01$ and -0.04 s^{-1}) are added for reference.

wake structures, similar to those during previous gliding phase, were generated [Fig. 10(d), I-2 and II-2].

IV. CONCLUSIONS

Three-dimensional particle tracking velocimetry was used to characterize the free fall of various cones in three dimensions accurately; volumetric particle image velocimetry was used to get complementary insight on the flow. Quantitative description of the linear and angular velocities, as well as the acceleration, revealed four distinct patterns strongly modulated by the specific gravity SG and heterogeneity. These include (i) straight fall, (ii) regular oscillations, (iii) large rotations with inclined translations, and (iv) tumbling. Cones with $SG \gtrsim 6$ exhibited straight fall (pattern 1) regardless of the mass distribution. Homogeneous cones with $SG < 3$ showed sinusoidal oscillations (pattern 2). Heterogeneous cones with $SG < 3$ resulted in large rotations greater than $\theta_{\max} > \pi/2$ (pattern 3). The heterogeneous cone with the largest distance between the center of mass and geometrical centroid $|\bar{x} - x_c|$ exhibited tumbling with irregular motions (pattern 4). Close inspection of the heterogeneous cones with $SG < 3$ revealed four distinct stages, namely, no inclination, large rotation, inclined translation (gliding), and backward rotation. Comparatively, a large $|\bar{x} - x_c|$ triggered additional torque during the oscillation that promoted a maximum oscillating angle of $\theta_{\max} > \pi/2$. Flow inspection of this pattern revealed that the stages may promote particular mixing in the induced flow.

Finally, the study provides insight for a comprehensive characterization of cones with various degrees of mass heterogeneity and distinct geometry for the design of objects with stable, highly unstable, and customized free falls. It is worth pointing out that current knowledge of hydrodynamic force on cones as a function of the angle of attacks is limited, which inhibits quantitative analysis with quasistatic models. Future work will include systematic characterization of hydrodynamic loads on static cones and under irregular motions, as well as a detailed description of the effects of the center of mass for a given bulk density.

ACKNOWLEDGMENT

This work was supported by the Department of Mechanical Science and Engineering, University of Illinois at Urbana-Champaign.

-
- [1] S. M. Herrington, J. T. Renzelman, T. D. Fields, and O. A. Yakimenko, Vertical wind-tunnel testing of steerable cruciform parachute system, *J. Aircraft* **56**, 747 (2018).
 - [2] L. Wilson and T. C. Huang, The influence of shape on the atmospheric settling velocity of volcanic ash particles, *Earth Planet Sci. Lett.* **44**, 311 (1979).
 - [3] D. S. Green, The terminal velocity and dispersal of spinning samaras, *Am. J. Botany* **67**, 1218 (1980).
 - [4] J. C. Maxwell, On a particular case of the descent of a heavy body in a resisting medium, *Camb. Dublin Math. J.* **9**, 115 (1853).
 - [5] R. H. Magarvey and R. L. Bishop, Transition ranges for three-dimensional wakes, *Can. J. Phys.* **39**, 1418 (1961).
 - [6] A. Goldberg and B. H. Florsheim, Transition and Strouhal number for the incompressible wake of various bodies, *Phys. Fluids* **9**, 45 (1966).
 - [7] K. O. L. F. Jayaweera and B. J. Mason, The behaviour of freely falling cylinders and cones in a viscous fluid, *J. Fluid Mech.* **22**, 709 (1965).
 - [8] J. J. Miao, T. S. Leu, T. W. Liu, and J. H. Chou, On vortex shedding behind a circular disk, *Exp. Fluids* **23**, 225 (1997).
 - [9] M. Jenny, G. Bouchet, and J. Dušek, Nonvertical ascension or fall of a free sphere in a Newtonian fluid, *Phys. Fluids* **15**, L9 (2003).
 - [10] M. Horowitz and C. H. K. Williamson, Critical mass and a new periodic four-ring vortex wake mode for freely rising and falling spheres, *Phys. Fluids* **20**, 101701 (2008).
 - [11] M. Horowitz and C. H. K. Williamson, The effect of Reynolds number on the dynamics and wakes of freely rising and falling spheres, *J. Fluid Mech.* **651**, 251 (2010).
 - [12] S. B. Field, M. Klaus, M. G. Moore, and F. Nori, Chaotic dynamics of falling disks, *Nature (London)* **388**, 252 (1997).
 - [13] H. Zhong, S. Chen, and C. Lee, Experimental study of freely falling thin disks: Transition from planar zigzag to spiral, *Phys. Fluids* **23**, 011702 (2011).
 - [14] H. Zhong, C. Lee, Z. Su, S. Chen, M. Zhou, and J. Wu, Experimental investigation of freely falling thin disks. Part 1. The flow structures and Reynolds number effects on the zigzag motion, *J. Fluid Mech.* **716**, 228 (2013).
 - [15] E. Kanso, L. Heisinger, and P. Newton, Coins falling in water ERRATUM, *J. Fluid Mech.* **742**, 243 (2014).
 - [16] L. Vincent, W. S. Shambaugh, and E. Kanso, Holes stabilize freely falling coins, *J. Fluid Mech.* **801**, 250 (2016).
 - [17] T. Lam, L. Vincent, and E. Kanso, Passive flight in density-stratified fluids, *J. Fluid Mech.* **860**, 200 (2019).
 - [18] See Supplemental Material at <http://link.aps.org/supplemental/10.1103/PhysRevFluids.5.093801> for visualizations of the four patterns of motion of falling cones.
 - [19] J. R. Calvert, Experiments on the low-speed flow past cones, *J. Fluid Mech.* **27**, 273 (1967).
 - [20] T. Yaginuma and H. Ito, Drag and wakes of freely falling 60° cones at intermediate Reynolds numbers, *Phys. Fluids* **20**, 1 (2008).
 - [21] A. M. Hamed, Y. Jin, and L. P. Chamorro, On the transient dynamics of the wake and trajectory of free falling cones with various apex angles, *Exp. Fluids* **56**, 207 (2015).
 - [22] K. Amin, J. Mac Huang, K. J. Hu, J. Zhang, and L. Ristroph, The role of shape-dependent flight stability in the origin of oriented meteorites, *Proc. Natl. Acad. Sci. USA* **116**, 16180 (2019).
 - [23] M. K. Sharma and R. P. Chhabra, An experimental study of free fall of cones in Newtonian and Non-Newtonian media: drag coefficient and wall effects, *Chem. Eng. Process. Process Intensif.* **30**, 61 (1991).

- [24] P. Mishra, A. K. Tiwari, and R. P. Chhabra, Effect of orientation on the drag of a cone settling in a Bingham plastic fluid, *Particuology* **43**, 157 (2018).
- [25] C. Charles, T. Eriksen, J. O., D. L. Russell, W. Timothy, W. L. Thomas, L. S. Peter, W. B. John, and M. C. Andrew, Seaglider: a long-range autonomous underwater vehicle for oceanographic research, *IEEE J. Oceanic Eng.* **26**, 424 (2001).
- [26] B. Allotta, L. Pugi, F. Bartolini, A. Ridolfi, R. Costanzi, N. Monni, and J. Gelli, Preliminary design and fast prototyping of an autonomous underwater vehicle propulsion system, *Proc. Inst. Mech. Eng. M: J. Eng. Maritime Env.* **229**, 248 (2015).
- [27] Y. Kim and C. S. Peskin, 3-D Parachute simulation by the immersed boundary method, *Comput. Fluids* **38**, 1080 (2009).
- [28] P. Craven and G. Wahba, Smoothing noisy data with spline functions, *Numer. Math.* **31**, 377 (1978).
- [29] J.-T. Kim, S. Shen, S. L. DiMarco, Y. Jin, and L. P. Chamorro, Lagrangian acceleration in Rayleigh-Bnard convection at various aspect ratios, *Phys. Rev. Fluids* **3**, 113502 (2018).
- [30] J.-T. Kim, Y. Jin, and L. Chamorro, Dynamics of flexible plates and flow under impulsive oscillation, *J. Fluid. and Struct.* **87**, 319 (2019).
- [31] J.-T. Kim, J. Nam, S. Shen, C. Lee, and L. Chamorro, On the dynamics of air bubbles in RayleighBénard convection, *J. Fluid Mech.* **891** (2020).
- [32] S. F. Hoerner, *Fluid-Dynamic Drag* (Hoerner Fluid Dynamics, 1965).
- [33] J. E. Brunk, Flight dynamics of samara-type single-wing autorotors, doi: [10.13140/RG.2.2.19412.40320](https://doi.org/10.13140/RG.2.2.19412.40320).